Available online at www.sciencedirect.com
SCIENCE DIRECT®
Acta Materialia 53 (2005) 5401–5413
Acta MATERIALIA
www.actamat-journals.com

Temporal evolution of the nanostructure of Al(Sc,Zr) alloys: Part I – Chemical compositions of $Al_3(Sc_{1-x}Zr_x)$ precipitates

Christian B. Fuller [a,b], Joanne L. Murray [c], David N. Seidman [a,*]

[a] Department of Materials Science and Engineering, Northwestern University, 2220 Campus Drive, Evanston, IL 60208-3108, USA
[b] Rockwell Scientific, 1049 Camino Dos Rios, Thousand Oaks, CA 91360, USA
[c] Alcoa Inc., Alcoa Technical Center, Alcoa Ctr., PA 15069, USA

Received 16 April 2005; received in revised form 6 August 2005; accepted 12 August 2005

Abstract

Atom-probe tomography (APT) and high-resolution transmission electron microscopy are used to study the chemical composition and nanostructural temporal evolution of $Al_3(Sc_{1-x}Zr_x)$ precipitates in an Al–0.09 Sc–0.047 Zr at.% alloy aged at 300 °C. Concentration profiles, via APT, reveal that Sc and Zr partition to $Al_3(Sc_{1-x}Zr_x)$ precipitates and Zr segregates concomitantly to the α-Al/$Al_3(Sc_{1-x}Zr_x)$ interface. The Zr concentration in the precipitates increases with increasing aging time, reaching a maximum value of 1.5 at.% at 576 h. The relative Gibbsian interfacial excess (Γ_{Zr}^{Al-Sc}) of Zr, with respect to Al and Sc, reaches a maximum value of 1.24 ± 0.62 atoms nm^{-2} after 2412 h. The temporal evolution of $Al_3(Sc_{1-x}Zr_x)$ precipitates is determined by measuring the time dependence of the depletion of the matrix supersaturation of Sc and Zr. The time dependency of the supersaturation of Zr does not follow the asymptotic $t^{-1/3}$ law while that of Sc does, indicating that a quasi-stationary state is not achieved for both Sc and Zr.

Keywords: Al–Sc–Zr alloys; Precipitation; Microstructure; High-resolution electron microscopy; Three-dimensional atom-probe microscopy

1. Introduction

The temporal evolution of the nanostructure of aged Al(Sc,Zr) alloys is presented in two articles. Part I reports on the chemical compositions of $Al_3(Sc_{1-x}Zr_x)$ precipitates utilizing atom-probe tomography (APT) and high-resolution transmission electron microscopy (HREM), while Part II [1] presents the morphology and coarsening kinetics of $Al_3(Sc_{1-x}Zr_x)$ precipitates utilizing HREM and conventional transmission electron microscopy (CTEM). The present study is part of a research program to deduce relationships between the nanostructures of two-phase α-Al/$Al_3(Sc_{1-x}Zr_x)$ alloys and mechanical properties at ambient and elevated temperatures [2–23], in particular creep.

Precipitation strengthened Al(Sc)-based alloys are candidates for use in the aerospace and ground vehicle industries, because of their excellent creep properties [4,11,14,17]. Upon aging, elastically hard and coherent Al_3Sc precipitates form with an $L1_2$ structure [24], a lattice parameter misfit of 1.34% with Al at ambient temperature [12], a melting temperature of 1320 °C [25], and a maximum Sc solid-solubility of 0.23 at.% in the primary solid-solution (α) at the eutectic temperature, 660 °C [24]. Elagin et al. [26] first suggested that Zr could substitute for Sc in Al_3Sc precipitates, and that aging alloys above 300 °C produces a longer hardness plateau for an Al–0.24 Sc–0.04 Zr at.% alloy than for an Al–0.24 Sc at.% alloy. After aging an Al–0.24 Sc–0.04 Zr at.% alloy at 450 °C, a bimodal distribution of precipitates was observed [26]. Energy dispersive X-ray (EDX) analyses demonstrated that the larger precipitates were Al_3Sc and the smaller precipitates were $Al_3(Sc_{1-x}Zr_x)$, and that both precipitate types had the $L1_2$ crystal structure [26].

Later Toropova et al. [27] utilized EDX to determine quantitatively the Sc and Zr concentrations within the

* Corresponding author. Tel.: +1 847 491 4391.
E-mail address: d-seidman@northwestern.edu (D.N. Seidman).

1359-6454/$30.00
doi:10.1016/j.actamat.2005.08.016

precipitates. Their research indicated that a Sc/Zr ratio (at.%/at.%) greater than unity resulted in the Al_3Sc ($L1_2$) phase, while a ratio less than unity resulted in the Al_3Zr (DO_{23}) phase. Kamardinkin [28] reported that the maximum solid-solubility of Zr in the Al_3Sc phase is 13.7–14.2 at.%, and the maximum solid-solubility of Sc in the Al_3Zr phase is 3 at.%. Increasing the Zr/Sc ratio in the alloy results in an increase in the Zr/Sc ratio in the $Al_3(Sc,Zr)$ precipitates, until a maximum concentration of ca. 12% Zr is achieved. Once the maximum Zr concentration is reached, additional Zr results in the formation of the Al_3Zr phase (DO_{23}).

Harada and Dunand [12] observed a similar trend for the effects of Zr additions on polycrystalline specimens of the Al_3Sc intermetallic. Zirconium can replace up to 50% of the Sc atoms in the Al_3Sc ($L1_2$) phase, while additional Zr results in the formation of Al_3Zr (DO_{23}). Harada and Dunand, in agreement with [27,28], found that up to 5 at.% Sc is soluble in Al_3Zr. Zirconium substitutions decrease the lattice parameter of Al_3Sc precipitates [12], resulting in a decrease in the lattice parameter misfit with the α-Al matrix from 1.34% for Al_3Sc to 1.07% for $Al_3(Sc_{0.5}Zr_{0.5})$ at 24 °C, and from 1.05% for Al_3Sc to 0.78% for $Al_3(Sc_{0.5}Zr_{0.5})$ at 300 °C. The lattice parameter expansion between 24 and 300 °C was calculated from the thermal expansivity of Al_3Sc (0.415%) [29] and Al (0.699%) [30], assuming Vegard's law [31] for the lattice parameter of the α-Al solid-solution.

The chemical composition of $Al_3(Sc_{1-x}Zr_x)$ precipitates has been investigated employing analytical TEM [32,33] and a combination of TEM and APT [34]. All three papers indicated that Zr is present within $Al_3(Sc_{1-x}Zr_x)$ precipitates, in agreement with [12,27], and that Zr was detected at the α-Al/$Al_3Sc_{1-x}Zr_x$ interfaces, in agreement with recent atomistic simulations [35]. In the case of Vetrano and Henager [32], the amount of Zr at the interface could not be quantified due to the small precipitate radius (<15 nm). Forbord et al. [34], however, utilized APT to find an ~8–10 at.% Zr concentration at the α-Al/$Al_3Sc_{1-x}Zr_x$ interfaces aged at 475 °C for 15 h. Vetrano and Henager [32] suggested that the Zr at the interface acted as a barrier to Sc diffusion across the interface, which in turn led to a reduction in the coarsening rate of Al_3Sc precipitates. An extensive review on Al–Sc-based alloys was recently published [36].

An analytical model describing diffusion-limited coarsening for a binary alloy was developed by Lifshitz and Slyozov [37] and Wagner [38] (LSW). The assumptions of the LSW model are [39,40]: (i) the linearized Gibbs–Thomson equation is valid; (ii) no elastic interactions occur among precipitates, i.e., the precipitate volume fraction is essentially zero; (iii) diffusion fields of precipitates do not overlap; (iv) dilute solution theory obtains; (v) coarsening occurs in a stress-free matrix; (vi) precipitates have a spherical morphology; (vii) precipitates form with the composition given by the equilibrium phase diagram; and (viii) a stationary state, $\partial C_i/\partial t = 0$, obtains, where C_i is the concentration of solute and t is time. An implicit assumption of LSW theory is that coarsening occurs via an evaporation–condensation model that involves a single atom evaporating from a small precipitate and condensing on a larger precipitate. The LSW model predicts that as the aging time, t, approaches infinity, three asymptotic solutions are obtained: (i) precipitate number density is proportional to t^{-1}; (ii) the mean, $\langle R\rangle$, precipitate radius is proportional to $t^{1/3}$; and (iii) the matrix supersaturation is proportional to $t^{-1/3}$. These time dependencies also obtain for n-component alloys, albeit with different rate constants [41,42]. The time dependencies of $\langle R\rangle$ and number density are presented and discussed in Part II [1], while the time dependence of the supersaturation of Sc and Zr is considered in Part I.

Umantsev and Olson [41] described an analytical approach for determining a quasi-stationary state, $\partial C_i/\partial t \approx 0$, diffusion-limited coarsening rate in multicomponent systems, without capillary effects. The case of quasi-stationary state coarsening in ternary systems was addressed in detail by Kuehmann and Voorhees [42], including capillary effects. Collectively the analytical analyses of Umantsev and Olson [41] and Kuehmann and Voorhees [42] are denoted the UOKV model. Kuehmann and Voorhees derive a relationship between solute composition within the matrix, C_i^α, and aging time (assuming a dilute solution and with the off-diagonal terms of the diffusion tensor equal to zero), which is given by

$$[C_i^\alpha(t) - C_i^\alpha(t\to\infty)] = \frac{2\gamma V_m (C_i^\beta - C_i^\alpha)}{R_g T[C_{Sc}^\alpha(1-k_{Sc})^2 + C_{Zr}^\alpha(1-k_{Zr})^2]} k_{exp}^{1/3} t^{-1/3}; \quad (1)$$

where C_i^α is the equilibrium solid-solubility of the ith component in the matrix, the superscripts α and β refer to the matrix and precipitate phases, respectively, V_m is the molar volume of the precipitate ($1.038\times10^{-5}\ m^3\ mol^{-1}$), calculated from $V_m = N_a a^3/4$ (N_a is Avogadro's number and $a = 0.410$ nm is the lattice parameter of $Al_3(Sc_{0.9}Zr_{0.1})$) [12], γ is an isotropic interfacial free energy, k_{exp} is the experimentally determined coarsening rate constant, obtained by plotting $\langle R(t)\rangle^3$ versus t; R_g is the ideal gas constant, T is the absolute temperature, and k_i is the distribution coefficient of the ith species between the α and β phases and is defined by C_i^β/C_i^α. The quantity $[C_i^\alpha(t) - C_i^\alpha(t\to\infty)]$ is denoted the matrix supersaturation of a solute i.

APT is the only experimental method that is presently capable of obtaining a direct quantitative measurement of the matrix supersaturation as a function of time, without chemical standards. In this study, we use APT to examine the heterophase interfaces in Al(Sc,Zr) ternary alloys in the presence of segregating solute atoms. The objectives of this research are: (i) to determine whether $Al_3(Zr_{1-x}Sc_x)$ precipitates exist within the alloy aged at 300 °C and their mechanism of formation; (ii) to measure the partitioning of Sc and Zr between the α-Al matrix and $Al_3(Sc_{1-x}Zr_x)$

precipitates as a function of aging time; (iii) to measure the relative Gibbsian interfacial excess of Zr with respect to Al and Sc at α-Al/$Al_3(Sc_{1-x}Zr_x)$ interfaces; and (iv) to determine the temporal evolution of the composition of $Al_3(Sc_{1-x}Zr_x)$ precipitates.

2. Phase equilibria of the Al–Sc–Zr system

In the binary Al–Zr system, the intermetallic phase that coexists in stable equilibrium with α-Al is Al_3Zr, whose crystal structure is $D0_{23}$, a superstructure of $L1_2$. A phase with an Ll_2 structure can also occur in Al–Zr alloys as a coherent metastable precipitate. Quantitative phase boundary data for metastable Al_3Zr ($L1_2$) are not available; based, however, on the stability of the metastable Al_3Zr ($L1_2$) phase, it appears that its liquidus and solvus boundaries lie just below their equilibrium counterparts.

The metastable Al_3Zr phase is isomorphous with the stable equilibrium phase of the Al–Sc system, Al_3Sc, whose liquidus and solvus have been carefully measured [43]. In ternary Al–Sc–Zr alloys, Sc and Zr substitute freely in $Al_3(Sc,Zr)$ ($L1_2$): as noted, ca. 12 at.% Zr dissolves in Al_3Sc ($L1_2$) at 550–600 °C, while only about 5 at.% Sc dissolves in Al_3Zr ($D0_{23}$) [28].

Two ternary phase diagrams are plotted in Figs. 1 and 2: both superimpose calculated isothermal sections from 300 to 400 °C. Fig. 1 shows the three-phase equilibria among α-Al, $Al_3(Sc,Zr)$ ($L1_2$), and Al_3Zr ($D0_{23}$), together with the compositions of the investigated alloys. According to the calculated phase diagram, three of our alloys are in the two-phase field α-Al plus $Al_3(Sc,Zr)$, and one is in the three-phase field. In practice, all our alloys exhibit only two phases for kinetic reasons. Therefore, in Fig. 2 the stable $Al_3(Sc,Zr)$ ($D0_{23}$) phase is suppressed and the metastable extension of the α-Al plus $Al_3(Sc,Zr)$ phase field is shown, with tie-lines. In Part II [1], we present experimental evidence that $Al_3(Sc,Zr)$ (DO_{23}) phase is not present in any of the Al(Sc,Zr) alloys we aged between 300 and 375 °C. Additionally, the Al–0.09 Sc–0.047 Zr at.% alloy indicated in Figs. 1 and 2 is the only alloy discussed in this article, while the other alloys are discussed in Part II [1].

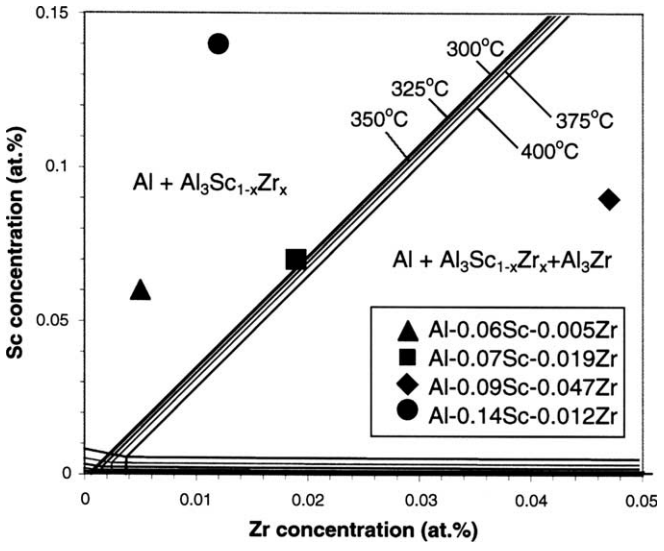

Fig. 1. Isothermal sections of a calculated ternary phase diagram for the Al(Sc,Zr) system in the Al-rich corner, with up to three equilibrium phases.

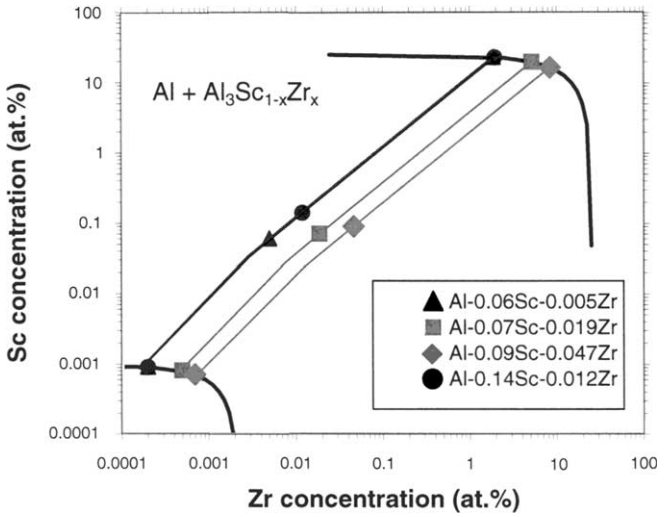

Fig. 2. Tie-lines for a calculated ternary phase diagram for the Al(Sc,Zr) system in the Al-rich corner at 300 °C, assuming one equilibrium precipitate phase, $Al_3(Sc_{1-x}Zr_x)$.

3. Experimental methods

3.1. Sample preparation

Al(Sc,Zr) alloys were produced by dilution casting Al–1.2 at.% Sc and Al–5.0 Zr at.% master alloys with 99.99 at.% Al. Charges for castings were heated in air in a resistively heated furnace to 720 °C, stirred to ensure complete mixing, and cast into a graphite mold resting on a large copper platen to encourage directional solidification at a rate of ~25 °C s^{-1}. The solidification rate was determined from the average value of two thermocouples residing 2.5 cm from the bottom and top of two neighboring channels in the mold. A coating of boron nitride on the graphite mold prevented interactions of the aluminum ingot with the graphite mold. In Table 1, the composition, calculated volume fraction, and Sc/Zr (at.% and wt.%) ratios of the Al(Sc,Zr) alloy investigated in Part I are listed. All bulk compositions were determined utilizing chemical analysis (Galbraith Laboratories, Knoxville, TN) and are given in at.%, unless otherwise noted.

The alloy was homogenized at 648 °C for 72 h, within the α-single-phase region, and then water quenched to 24 °C. Samples were aged at 300 °C for 0.25, 4.5, 72, 288, 576, or 2412 h to obtain $Al_3(Sc_{1-x}Zr_x)$ precipitates. To prevent precipitation during storage, the APT specimens were stored in liquid nitrogen between the homogenization and aging treatments.

Table 1
Characteristics of the Al(Sc,Zr) alloy investigated

Alloy (at.%)	Sc (wt.%)	Zr (wt.%)	Volume fraction (V_V) of $Al_3(Sc,Zr)$[a]	Sc/Zr (at.%/at.%) in $Al_3(Sc,Zr)$	Sc/Zr (wt.%/wt.%) in $Al_3(Sc,Zr)$
Al–0.09 Sc–0.047 Zr	0.15	0.16	0.0070	1.9	0.94

[a] Determined from calculated phase equilibria data at 300 °C.

TEM samples were fabricated by punching 3 mm diameter discs from 120 to 200 μm thick foils, which were produced by mechanical thinning. The 3-mm diameter discs were then jet electropolished (Struers Tenupol-5) employing a solution of 5 vol.% perchloric acid in methanol at −30 °C. HREM was performed utilizing a JEOL 4000 EXII (Argonne National Laboratory) operating at 200 kV. HREM samples were oriented along the ⟨100⟩ zone axis and precipitates were imaged with an aperture around the incident beam and the eight lowest order superlattice reflections of $Al_3(Sc_{1-x}Zr_x)$ ($L1_2$). This technique results in the imaging of the lattice planes in the $Al_3(Sc_{1-x}Zr_x)$ precipitates, but not in the α-Al matrix, thereby yielding distinct α-Al/$Al_3(Sc_{1-x}Zr_x)$ heterophase interfaces.

APT sample blanks were produced by drawing wires to a diameter of 250 μm. After performing the aging treatments, APT blanks were electropolished by a two-stage procedure at room temperature, to yield the requisite sharp needle-like geometry. First, a solution of nitric acid with a few drops of water was utilized for rough polishing. For the final electropolishing, a solution of 2 vol.% perchloric acid in 2-butoxyethanol was used. APT analyses were performed in a background vacuum of 10^{-9} Pa, at a tip temperature of 30 K, a pulse fraction (pulse voltage/steady-state dc voltage) of 18–20%, and a pulse frequency of 1.5 kHz, to obtain an average detection rate of 0.006–0.03 ions pulse^{-1}.

3.2. Atom-probe tomograph data analysis

Small volumes of the alloy are reconstructed from APT data employing *ADAM 1.5*, a visualization and analytical program developed at Northwestern University [44–49], for analyzing APT data. Employing *ADAM 1.5*, the reconstructed data are scaled laterally using a 60% detection efficiency for the average atomic density of the α-Al matrix (60 atoms nm^{-3}), while depth scaling is performed using the known interplanar spacings for specific $\{hkl\}$ planes. The error in concentration is given by the standard deviation, σ, for counting statistics

$$\sigma = \sqrt{\frac{C_i(1-C_i)}{N_{\text{atoms}}}}, \tag{2}$$

where C_i is the measured atomic concentration of species i and N_{atoms} is the total number of atoms within each bin of a proximity histogram [49].

A proximity histogram (or proxigram) [47–51] is constructed to calculate atomic concentrations relative to a defined isoconcentration surface, in 3D reconstructions of APT data. The proxigram is a profile of local atomic concentrations as a function of proximity to an isoconcentration surface, which can be calculated independent of the topological complexity of a precipitate. In this article, an isoconcentration surface with a threshold value of 18 at.% Sc is used to define the location of all α-Al/$Al_3(Sc_{1-x}Zr_x)$ heterophase interfaces for each aging treatment. With the heterophase interfaces so defined, the atomic concentration of each atomic species is calculated in parallel for all the heterophase interfaces in an analysis volume, as a function of distance from the interfaces. Proxigrams, therefore, produce spatially averaged concentration profiles that are independent of the morphology and complexity of an isoconcentration surface [47].

A correction was performed to account for the background noise in the mass spectra of APT analyses. First, the relative amount of noise contained within the width of each solute element peak of the mass spectrum was determined by calculating the ratio of the counts contained within each solute atom peak to the counts associated with the background level. A percentage of noise for each solute element within the matrix and precipitate phases is then determined from the peak-to-background ratio. The corrected solute concentration is calculated by multiplying the solute concentration by one minus the percentage of noise for each solute element; e.g., for the 18 at.% isoconcentration surface, (18 at.% Sc)(1 − 0.33) = 12 at.% Sc.

4. Results

4.1. High-resolution electron microscopy (HREM)

Aging of the Al–0.09 Sc–0.047 Zr at.% alloy at 300 °C produces precipitates with a radius ⩽2.5 nm. Figs. 3(a)–(d) compare the temporal evolution of precipitate morphology as a function of aging time (72, 288, 576, or 2412 h) at 300 °C, as shown by HREM images recorded along the ⟨100⟩ zone axis. After aging for 72 h, the precipitate facets are not well defined, while for times >288 h, the presence of facets parallel to the {100} and {110} planes are observed around a portion of each precipitate, Fig. 3. Fig. 3(c) exhibits precipitates with the highest degree of faceting, but the entire precipitate is not faceted. Examination of the inset diffraction pattern (Fig. 3(a)) detects only FCC and $L1_2$ reflections, but no reflections due to a DO_{23} crystal structure.

Table 2 compares ⟨R⟩ and the number of precipitates counted, as determined from HREM images. The mean radius increases slightly with increasing aging time, but

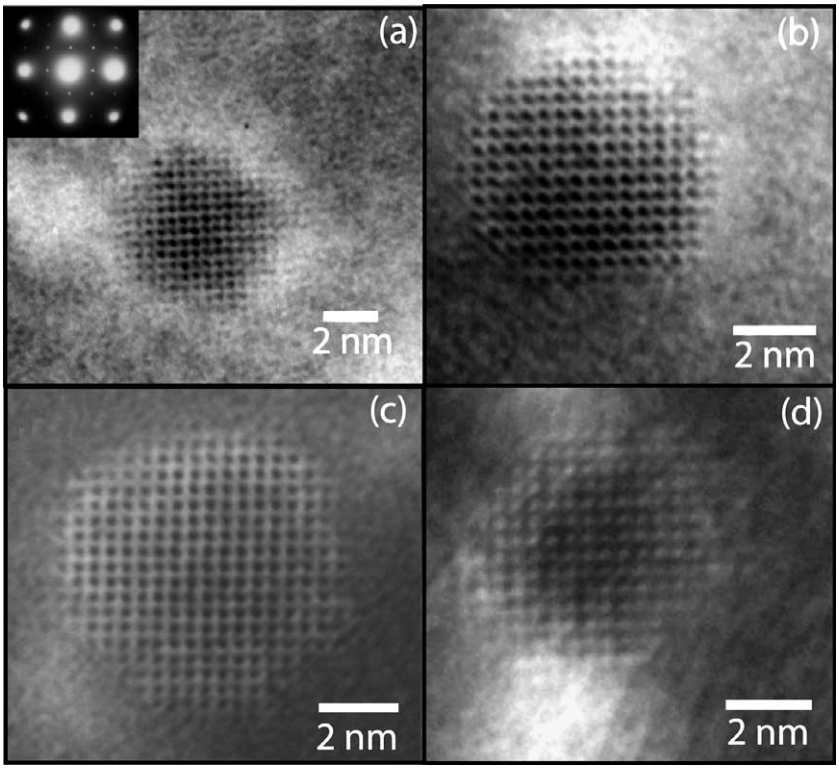

Fig. 3. A comparison of precipitate morphologies employing HREM images ([1 0 0] zone axis) of an Al–0.09 Sc–0.047 Zr alloy aged at 300 °C for: (a) 72; (b) 288; (c) 576; or (d) 2412 h.

Table 2
Evolution of mean precipitate radius, $\langle R \rangle$, of $Al_3(Sc_{1-x}Zr_x)$ precipitates as a function of aging time at 300 °C; determined from HREM images employing the eight lowest order superlattice reflections of the $L1_2$ structure

Aging time (h)	Mean precipitate radius (nm), $\langle R \rangle$	Number of precipitates counted
72	2.1 ± 0.1	127
288	2.3 ± 0.1	121
576	1.9 ± 0.2	272
2412	2.3 ± 0.1	186

Error in $\langle R \rangle$ is one standard deviation (σ) of the precipitate size distribution.

takes a slight deviation at 576 h due to the presence of small precipitates, Fig. 3(c). The high stability of $Al_3(Sc_{1-x}Zr_x)$ precipitates against coarsening at 300 °C is shown by the small change in $\langle R \rangle$ (12% increase) after 2340 h of aging; in contrast, $\langle R \rangle$ in the binary Al–0.18 Sc at.% alloy increases by 63% for a 344 h increase in aging time [7].

Precipitate size distributions (PSDs) were constructed by plotting the PSD function (g) as a function of the normalized precipitate radius (u = radius/mean radius), Fig. 4. The distributions were obtained from HREM images for samples aged at 300 °C for 72, 288, 576, or 2412 h, and are shown in comparison to the PSDs for LSW and Brailsford and Wynblatt (BW) [52] models. With increasing aging time, the PSD width decreases and the peak height increases; thus, the PSDs are not self-similar. Additionally, the PSDs exhibit a unimodal precipitate distribution and not a bimodal distribution, as was reported for Al(Sc,Zr) alloys aged at 450 °C [26].

4.2. Atom-probe tomography (APT)

4.2.1. As-quenched and early aging times

After the homogenization heat treatment, Sc (Fig. 5(a)) or Zr (Fig. 5(b)) clusters are not visually apparent in an atomic reconstruction of a $16 \times 16 \times 100$ nm^3 volume containing >933,500 atoms. The α-Al matrix compositions for the as-quenched alloy are 0.103 ± 0.003 at.% Sc and 0.041 ± 0.002 at.% Zr. After aging at 300 °C for 0.28 h, the presence of atomic clusters within a $14 \times 14 \times 89$ nm^3 volume containing over 594,200 atoms is still not obvious visually. The α-Al matrix compositions for the 0.28 h aging treatment are 0.108 ± 0.004 at.% Sc and 0.055 ± 0.003 at.% Zr. Thus, the α-Al matrix compositions of Sc and Zr are essentially unchanged between the as-quenched and 0.28 h conditions.

4.2.2. Coarsening

After aging at 300 °C for 4.5 h, two precipitates rich in Sc atoms are detected (Fig. 6(a)), while Zr atoms (Fig. 6(b)) appear to be randomly distributed throughout the α-Al matrix; the latter is a qualitative observation. A profile of solute–atom concentrations with respect to the α-Al/$Al_3(Sc_{1-x}Zr_x)$ interface is displayed in a composite proxigram, Fig. 7.

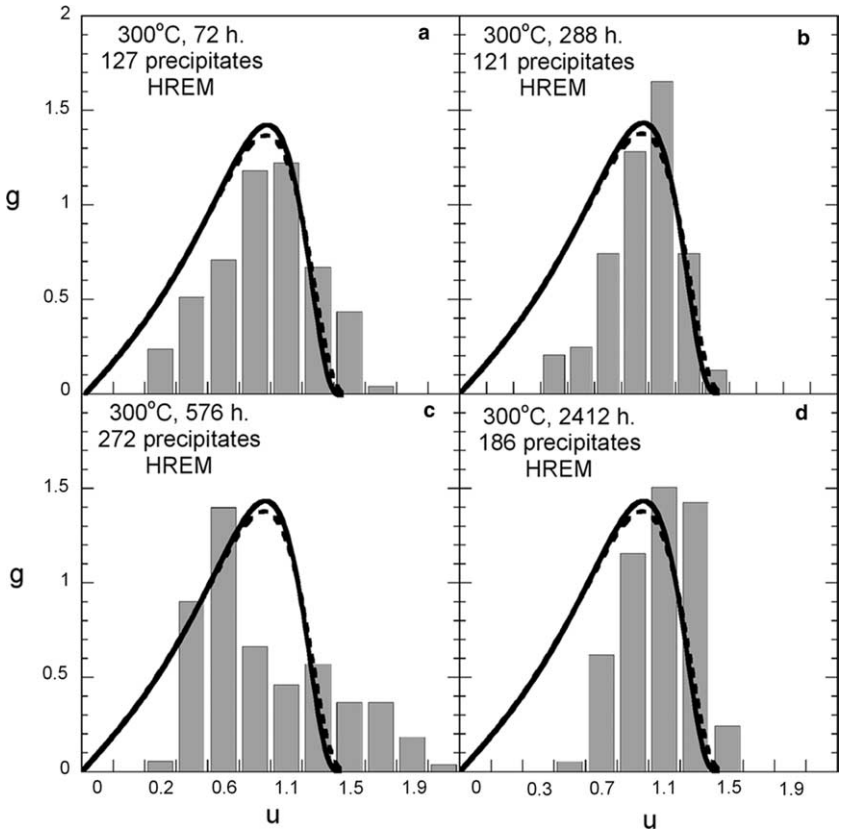

Fig. 4. A comparison of precipitate size distributions (PSDs), where the PSD function (g) is plotted as a function of normalized radius (u = radius/mean radius), as determined from HREM images ([1 0 0] zone axis) of an Al–0.09 Sc–0.047 Zr alloy aged at 300 °C for: (a) 72; (b) 288; (c) 576; or (d) 2412 h. The predictions of the LSW (solid line) [37,38] and BW (dashed line) [52] models are shown for comparison.

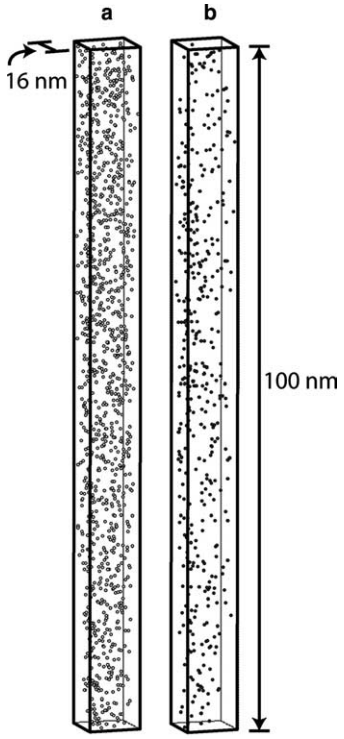

Fig. 5. Three-dimensional atom-by-atom reconstruction of an Al–0.09 Sc–0.047 Zr alloy homogenized at 648 °C for 72 h and water quenched to 24 °C; the Sc atoms are displayed in (a) and the Zr atoms in (b). The analysis volume measures $16 \times 16 \times 100$ nm^3 and contains 933,500 atoms.

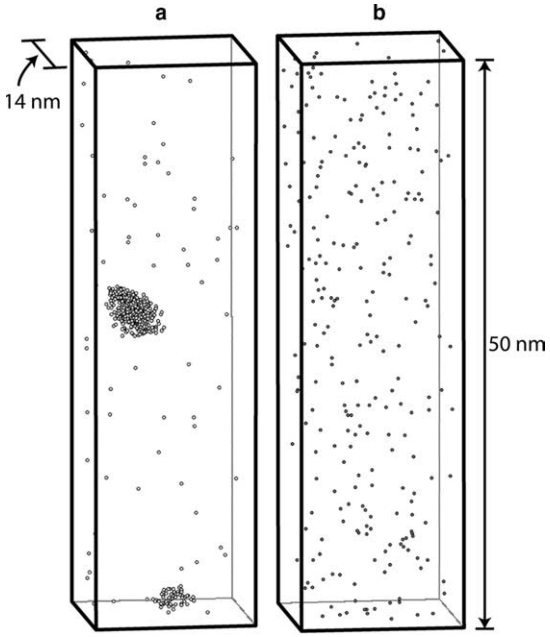

Fig. 6. Three-dimensional atom-by-atom reconstruction, measuring $14 \times 14 \times 50$ nm^3 and containing 358,000 atoms, of an Al–0.09 Sc–0.047 Zr alloy aged at 300 °C for 4.5 h, displaying (a) Sc and (b) Zr atoms. There are two $Al_3(Sc_{1-x}Zr_x)$ precipitates in (a).

The precipitate and α-Al phase compositions are determined from the plateau regions of each proxigram. Table 3 lists the precipitate composition as a function of aging time. From the α-Al matrix and α-Al/$Al_3(Sc_{1-x}Zr_x)$ compositions, a partitioning ratio (average atomic concentration in $Al_3(Sc_{1-x}Zr_x)$ divided by the average atomic concentration in α-Al) for Sc and Zr is calculated, Table 4. Clear partitioning of Sc and Zr to $Al_3(Sc_{1-x}Zr_x)$ is evident, after aging for 4.5 h. An enlarged view of the Zr concentration profile is shown in Fig. 7(b), and segregation of Zr atoms at the α-Al/$Al_3(Sc_{1-x}Zr_x)$ heterophase interface is evident.

Segregation is quantified by the relative Gibbsian interfacial excess of Zr with respect to Al and Sc, Γ_{Zr}^{Al-Sc}, which is independent of the position of the dividing surface. The Gibbsian interfacial excess is defined as the concentration of a given atomic species per unit area (planar area of an interface), and for a ternary alloy it is given by [53,54]

$$\Gamma_{Zr}^{Al-Sc} = \Gamma_{Zr} - \Gamma_{Sc}\left(\frac{C_{Al}^{\alpha}C_{Zr}^{\beta} - C_{Al}^{\beta}C_{Zr}^{\alpha}}{C_{Al}^{\alpha}C_{Sc}^{\beta} - C_{Al}^{\beta}C_{Sc}^{\alpha}}\right) - \Gamma_{Al}\left(\frac{C_{Zr}^{\alpha}C_{Sc}^{\beta} - C_{Zr}^{\beta}C_{Sc}^{\alpha}}{C_{Al}^{\alpha}C_{Sc}^{\beta} - C_{Al}^{\beta}C_{Sc}^{\alpha}}\right), \quad (3)$$

where C_i^l is the mean concentration of Zr, Sc, or Al in the α-Al and β-[$Al_3(Sc_{1-x}Zr_x)$] phases, respectively, and Γ_{Zr}, Γ_{Sc}, and Γ_{Al} are the measured Gibbsian interfacial excesses. The quantity Γ_i is calculated by measuring the area under a composition profile near an interface, and multiplying by the average atomic density of α-Al (60 atom nm^{-3}) [55]. For the 4.5 h aging treatment, the areas utilized to calculate Γ_{Zr}, Γ_{Sc}, and Γ_{Al} are indicated in Fig. 7 [48]. In Fig. 7, note that Γ_{Sc} and Γ_{Zr} are positive, while Γ_{Al} is negative, and that a majority of the Zr atoms reside to the right of the α-Al/$Al_3(Sc_{1-x}Zr_x)$ heterophase interface; i.e., inside the $Al_3(Sc_{1-x}Zr_x)$ precipitates. Utilizing the data in Fig. 7, the relative Gibbsian interfacial excess, Eq. (3), has small contributions from the second

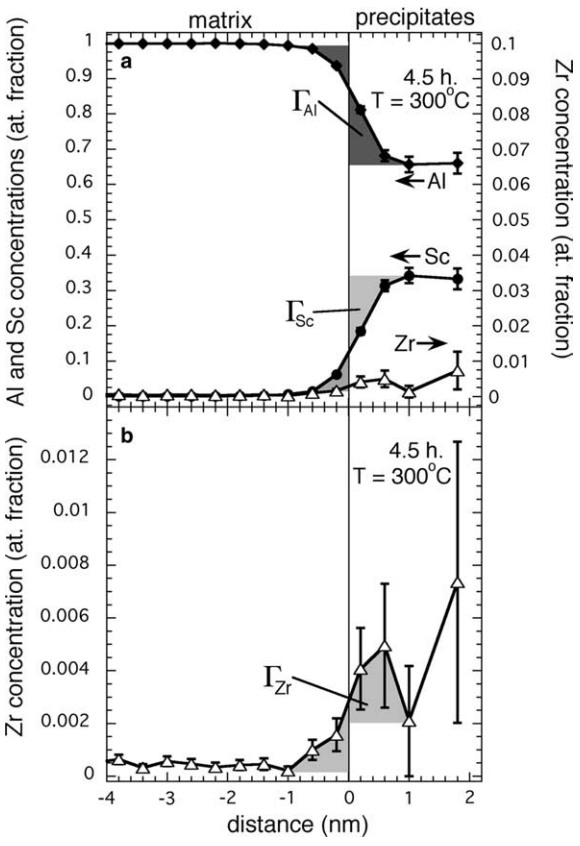

Fig. 7. (a) Proxigrams for Al, Sc and Zr concentrations as a function of distance (nm) with respect to the α-Al/$Al_3(Sc_{1-x}Zr_x)$ heterophase interface for an Al–0.09 Sc–0.047 Zr alloy aged at 300 °C for 4.5 h and (b) An enlargement of the Zr proxigram. The error bars correspond to ±σ values. The shading illustrates the Gibbsian excess quantities, Γ_i. This proxigram is for six $Al_3(Sc_{1-x}Zr_x)$ precipitates that are contained in a volume of 684,000 atoms.

Table 3
Evolution of precipitate composition and Sc/Zr ratio as a function of aging time at 300 °C

Aging time (h)	Number of precipitates	Al (at.%)	Sc (at.%)	Zr (at.%)	Sc/Zr (at.%/at.%)
4.5	6	67.1 ± 1.2	32.5 ± 1.2	0.4 ± 0.2	81 ± 40
72	11	69.2 ± 0.8	30.4 ± 0.8	0.4 ± 0.1	76 ± 19
288	15	69.0 ± 0.5	30.0 ± 0.4	1.0 ± 0.1	30 ± 3
576	10	70.7 ± 0.6	27.8 ± 0.6	1.5 ± 0.2	19 ± 3
2412	6	71.3 ± 0.7	27.5 ± 0.7	1.2 ± 0.2	23 ± 4

The uncertainties correspond to ±σ values.

Table 4
Evolution of Sc and Zr partitioning ratios (atomic concentration in precipitate/atomic concentration in matrix) and relative Gibbsian interfacial excess of Zr with respect to Al and Sc, Γ_{Zr}^{Al-Sc}, as a function of aging time at 300 °C

Aging time (h)	Sc partitioning ratio	Zr partitioning ratio	Γ_{Zr}^{Al-Sc} (atoms nm^{-2})
4.5	1492 ± 419	8 ± 4	0.20 ± 0.10
72	1302 ± 352	8 ± 3	0.35 ± 0.18
288	2012 ± 563	18 ± 5	0.39 ± 0.20
576	1859 ± 520	37 ± 12	1.17 ± 0.59
2412	1078 ± 301	31 ± 11	1.24 ± 0.62

The uncertainties correspond to ±σ values.

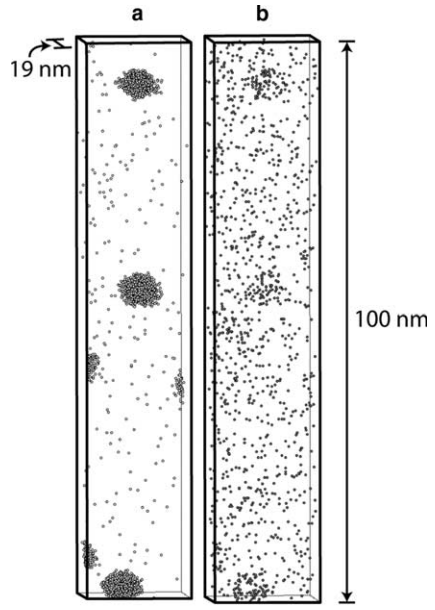

Fig. 8. Three-dimensional atom-by-atom reconstruction, measuring $19 \times 19 \times 100\ \text{nm}^3$ and containing 1,185,000 atoms, for an Al–0.09 Sc–0.047 Zr alloy aged at 300 °C for 288 h, displaying (a) Sc and (b) Zr atoms.

and third right-hand terms (averaging 1.9% and 0.1% of the first right-hand term, respectively); this is because of the sharpness of the interface. The $\Gamma_{\text{Zr}}^{\text{Al-Sc}}$ values listed in Table 4 are observed to increase systematically with increasing aging time, indicating that the system has not achieved a stationary state, but is most likely in a quasi-stationary state.

Unlike for earlier aging times, the Zr enrichment in the α-matrix is visually evident after aging for 288 h in the APT atomic reconstructions, Fig. 8. The quantitative degree of this enrichment is displayed in a corresponding composite proxigram, Fig. 9.

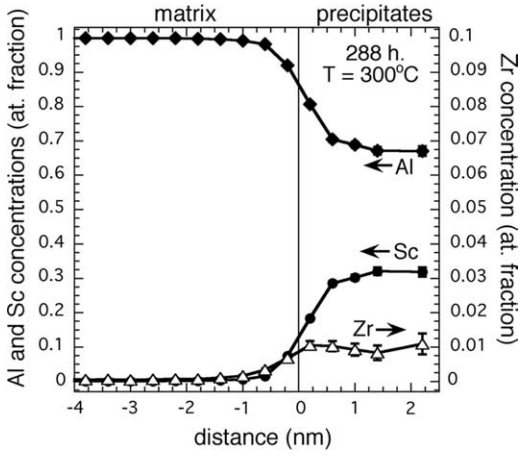

Fig. 9. Proxigrams of Al, Sc and Zr concentrations as a function of distance with respect to the α-Al/$Al_3(Sc_{1-x}Zr_x)$ interface for an Al–0.09 Sc–0.047 Zr alloy aged at 300 °C for 288 h. The error bars correspond to $\pm\sigma$ values. This proxigram was constructed from 15 $Al_3(Sc_{1-x}Zr_x)$ precipitates within a volume containing 4,380,000 atoms.

5. Discussion

5.1. Precipitate morphology

The equilibrium shape of Al_3Sc precipitates at 300 °C of an Al–0.18 Sc at.% alloy is a great rhombicuboctahedron, exhibiting 8{111}, 12{110} and 6{100} facets [3,7,56]. $Al_3(Sc_{1-x}Zr_x)$ precipitates are observed to have facets parallel to the {110} and {100} planes (Fig. 3), which appear to be nearly equal in length to the facets found for the binary Al–0.18 Sc at.% alloy. As stated in Section 1, Zr additions decrease the lattice parameter of the precipitate, which decreases concomitantly the α-Al/$Al_3(Sc_{1-x}Zr_x)$ interfacial misfit, thus increasing the radius to which precipitates can maintain coherency with the α-Al matrix. Assuming all of the Zr resides in the $Al_3(Sc_{1-x}Zr_x)$ precipitates, the lattice parameter misfit is calculated to change, at 300 °C, from 1.05% for α-Al/Al_3Sc to 0.87% for α-Al/$Al_3Sc_{0.67}Zr_{0.33}$, which is anticipated to change the interfacial free energy calculated for a two-phase alloy; this calculation is performed knowing the change in lattice parameter with Zr addition, at 24 °C, is $8.8 \pm 3.0 \times 10^{-5}$ nm at.% Zr^{-1} (where 3.0 denotes one standard deviation from the mean) [12], and the thermal expansivities between 24 and 300 °C are 0.415% for Al_3Sc [13] and 0.699% for Al [30], respectively. APT analyses indicate, however, that at 300 °C some of the Zr is still in α-Al matrix, so the actual misfit is greater than the calculated 0.87%, and may be closer to 1.02% (assuming a Zr concentration of 1.5 at.% in the precipitates).

HREM of an Al–0.09 Sc–0.047 at.% Zr precipitate aged at 350 °C for 2328 h exhibits a decrease in the amount of faceting parallel to the {100} and {110} planes, becoming approximately spheroidal (Fig. 10). This change in morphology is an indication that the precipitate interfacial free energies for the {100} and {110} planes have become approximately equal after aging at 350 °C; this is due to Zr segregation at the α-Al/$Al_3(Sc_{1-x}Zr_x)$ interface. Al_3Sc

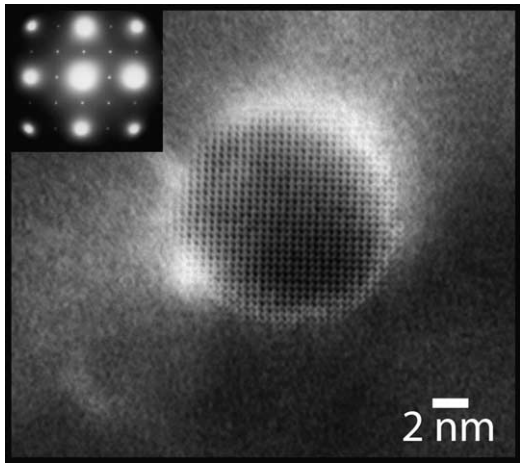

Fig. 10. A HREM image ([100] zone axis) of an $Al_3(Sc_{1-x}Zr_x)$ precipitate in an Al–0.09 Sc–0.047 Zr alloy aged at 350 °C for 2328 h.

precipitates are faceted when aged at 350 or 400 °C [7], so the change in precipitate morphology cannot be explained without the presence of Zr. Spheroidal precipitates are not observed for the 300 °C aging treatments (Fig. 3), because the concentration of Zr in the precipitate at 300 °C (for aging times <2412 h) is lower than the concentration needed to produce spheroidal precipitates.

5.2. Partitioning behavior of Al–0.09 Sc–0.047 Zr at.%

Table 3 demonstrates that there is an increase in the concentration of Zr in the precipitates with increasing aging time, and a concomitant decrease in Sc concentration. These changes are reflected in the partitioning ratios, Table 4. The Sc partitioning ratios, however, do not show a clear trend, since most of the partitioning ratios are equal within experimental error. The diffusivity of Sc in Al is over four orders of magnitude greater than that of Zr in Al at 300 °C [57,58], which implies that the Sc concentration is able to change significantly more rapidly than the Zr concentration.

5.3. Segregation of Zr at α-Al/$Al_3Sc_{1-x}Zr_x$ heterophase interfaces

The Sc and Zr concentration profiles (proxigrams) as a function of aging time at 4.5, 288, and 2412 h are compared in Fig. 11. Fig. 11(a) demonstrates that the Sc concentrations in the precipitates are slowly decreasing as a function of aging time, and the Zr concentrations are concomitantly increasing slowly, Fig. 11(b). The decrease in Sc with a concomitant increase in Zr indicates that Zr is substituting for Sc within the $Al_3(Sc_{1-x}Zr_x)$ precipitates, thereby increasing the value of x, Table 3. The average Sc concentration in the $Al_3(Sc_{1-x}Zr_x)$ precipitates ranges from 32.5 to 27.5 at.% Sc. Additionally, the Sc plus Zr concentration in the precipitates decreases from 32.9 at.% at 4.5 h to 28.7 at.% at 2412 h, as the Zr concentration is increasing with decreasing Sc concentration. This demonstrates that $Al_3(Sc_{1-x}Zr_x)$ precipitates nucleate with a Sc-rich composition, which decreases slowly with increasing time to achieve the requisite stoichiometric composition, where the Sc plus Zr concentrations equals 25 at.%. This is inconsistent with the LSW assumption of constant precipitate composition during coarsening of a binary alloy, but is consistent with the Kuehmann–Voorhees quasi-stationary state coarsening model for a ternary alloy, which permits the composition of the matrix and precipitate to evolve temporally during coarsening. The experimental observations of increasing Zr concentration with aging time also agree with the model prediction of Robson [59], who used a modified Kampmann–Wagner [60] N-model to predict that the Zr concentration in $Al_3(Sc_{1-x}Zr_x)$ precipitates increases during precipitation.

With increasing aging time, the Zr concentration at the α-Al/$Al_3(Sc_{1-x}Zr_x)$ heterophase interface increases (Fig. 11(b)), indicating that Zr atoms are migrating toward

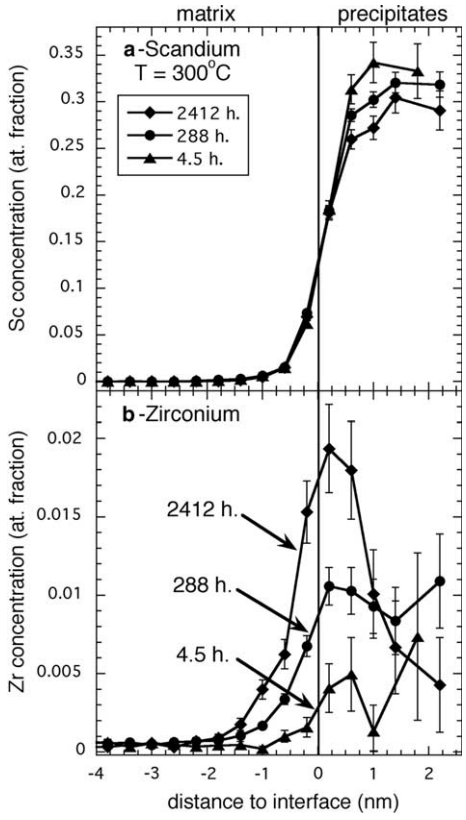

Fig. 11. A comparison of (a) Sc or (b) Zr concentrations as a function of distance with respect to the α-Al/$Al_3(Sc_{1-x}Zr_x)$ heterophase interface for an Al–0.09 Sc–0.047 Zr alloy aged at 300 °C for the indicated times. The 4.5 h aging time results are based on six $Al_3(Sc_{1-x}Zr_x)$ precipitates and a total of 684,000 atoms, the results for 288 h are based on 15 $Al_3(Sc_{1-x}Zr_x)$ precipitates and a total of 4,380,000 atoms, and the results for 2412 h are based on six $Al_3(Sc_{1-x}Zr_x)$ precipitates and a total of 607,000 atoms. The error bars correspond to $\pm\sigma$ values.

the interfacial region. The increase in segregation is quantified by a temporally increasing value of Γ_{Zr}^{Al-Sc}, Table 4. This is reasonable since Zr diffuses significantly slower [58] than Sc [57] in α-Al (e.g. at 300 °C for 288 h the root-mean-squared diffusion distance of Zr in Al is 6 nm and Sc in Al is 747 nm). A comparison of Fig. 11(a) with Fig. 11(b) demonstrates that the peak of Zr enhancement is at the periphery of the defined α-Al/$Al_3(Sc_{1-x}Zr_x)$ heterophase interface, thus $Al_3(Sc_{1-x}Zr_x)$ precipitates exhibit a Zr-rich concentric shell at or just inside this heterophase interface. For an ideal dilute solid-solution, the Gibbs adsorption isotherm is given by [61]

$$\Gamma_{Zr} = -\frac{C_{Zr}N_a}{RT}\left(\frac{\partial\gamma}{\partial C_{Zr}}\right). \quad (5)$$

Utilizing the values measured for the 2412 h aging time ($C_{Zr} = 3.92\times10^{-4}$ at. fr. at 573 K and $\Gamma_{Zr}^{Al-Sc} = 1.24\pm 0.62$ atoms nm^{-2}), the quantity $(\partial\gamma/\partial C_{Zr})$ is equal to -20.5 mJ m^{-2} (at. fr.)$^{-1}$. This implies an interfacial free energy decrease of -10 ± 5 mJ m^{-2}, which is a result of interfacial Zr segregation and is 6%, 5%, and 4% of the calculated α-Al/Al_3Sc interfacial free energies for the {100}, {111} and {110} facets, respectively; 160 mJ m^{-2}

for {100} and 185 mJ m^{-2} for {111} facets at 300 °C [56,62], and 226 mJ m^{-2} for the {110} orientation at 0 K [63].

5.4. Precipitate nucleation

In Part II [1], we demonstrate that the $Al_3(Sc_{1-x}Zr_x)$ precipitate number density increases with increasing Zr additions to an Al–Sc alloy, which is evidence that precipitates form on clusters containing Zr atoms. Precipitate nucleation could be either homogeneous or heterogeneous. Local composition fluctuations of solute elements would be the source of homogeneous nucleation. In contrast, heterogeneous precipitate nucleation would occur, for instance, on Sc–Sc, Sc–Zr, or Zr–Zr dimers in the α-Al matrix. In order for these dimers to play a role in heterogeneous nucleation, the dimers must have sufficient mobility to interact with other dimers, but the detailed kinetics are presently unknown. With increasing aging time, 4.5–2412 h, the value of Γ_{Zr}^{Al-Sc} increases concomitantly (Fig. 11(b)). At the longest aging time, 2412 h, the Zr concentration decreases as a function of distance from both sides of the α-Al/$Al_3(Sc_{1-x}Zr_x)$ heterophase interface (Fig. 11(b)), indicating that Zr diffuses from both the inside and outside of the $Al_3(Sc_{1-x}Zr_x)$ precipitates toward their peripheries. Therefore, a possible sequence of precipitate formation is postulated to be: (i) heterogeneous nucleation of Al_3Sc and/or $Al_3Sc_{1-x}Zr_x$ precipitates; and (ii) diffusion of Zr to Al_3Sc and/or $Al_3Sc_{1-x}Zr_x$ precipitates until the equilibrium stoichiometric composition is ultimately achieved. This is a simplified explanation of a precipitate's nucleation, growth and coarsening behavior, and therefore lattice kinetic Monte Carlo and cluster dynamic simulations are needed to unravel the atomistic details [35].

5.5. Coarsening kinetics

Fig. 12 displays the Sc and Zr concentrations in the α-Al matrix as a function of (time)$^{-1/3}$. The Sc concentration decreases nonlinearly between 0.28 and 4.5 h and thereafter it decreases linearly. The Zr concentration is approximately constant from 0.28 to 72 h, and then it also decreases linearly with increasing aging time. The extrapolated intercept on the ordinate axis (Fig. 12) corresponds to the equilibrium solute solid-solubility in the α-Al matrix, $C_i^{\alpha}(t \to \infty)$ (Eq. (1)). Table 5 compares the solute solid-solubility calculated using Fig. 12 with the predictions of the calculated phase diagram (assuming a two-phase alloy), indicating that the experimental concentrations are >15 times the calculated values. The difference between the two values can be attributed to: (1) an evolving precipitate composition (system has not achieved a stationary state); (2) an inaccuracy in the time exponent for coarsening (assumed to be −1/3 in Fig. 12); and/or (3) the model phase diagram calculations are not accurate.

The time exponent for coarsening in Eq. (1) can now be determined by plotting the matrix supersaturation as a function of aging time on a double-logarithmic plot and calculating the corresponding slope, Fig. 13. Utilizing a linear regression analysis, the time exponent for coarsening is determined to be −0.33 for Sc and −0.11 for Zr, as compared to −1/3 in Eq. (1). Hence, depletion of Sc from the matrix is close to the value of ca. −1/3, but Zr depletion is not. After 2412 h at 300 °C, the root-mean-squared diffusion distance of Sc in Al is 2162 nm [54] and only 18 nm for Zr in Al [56]; experimental values for D_0 and Q are listed in Table 6. The center-to-center interprecipitate distance, [17, Eq. (4)], for the Al–0.09 Sc–0.047 Zr at.% alloy aged at

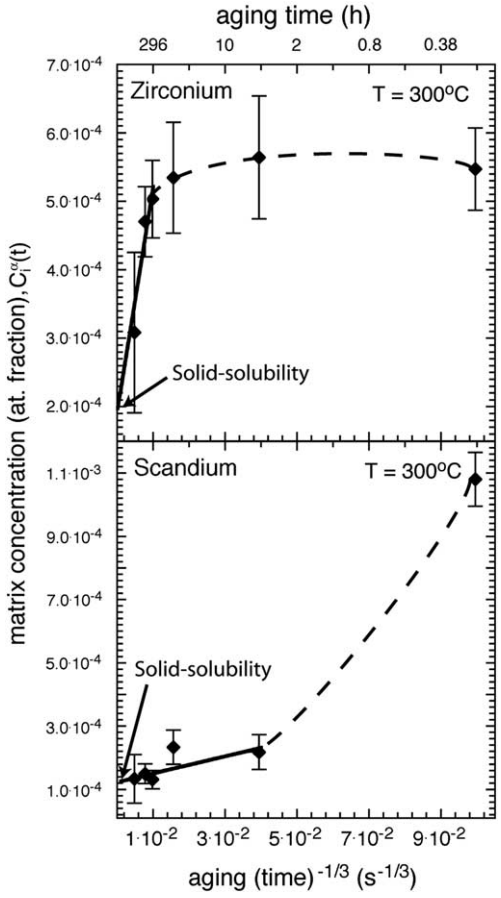

Fig. 12. Coarsening kinetics of an Al–0.09 Sc–0.047 Zr alloy as represented by the Sc and Zr matrix concentrations as a function of aging (time)$^{-1/3}$ at 300 °C, Eq. (1). A total of 8,516,000 atoms were employed to construct this plot. The error bars in this plot represent ±2σ values.

Table 5
Equilibrium matrix concentrations (at. fr.), C_e^{α}, of Sc and Zr as determined from the phase diagram, Fig. 2, and the ordinate intercept of Fig. 13, Eq. (5)

Solute element	C_e^{α} (at. fr.) calculated from phase diagram	C_e^{α} (at.fr.) measured from coarsening kinetics
Sc	7×10^{-6}	$1.2 \pm 0.3 \times 10^{-4}$
Zr	7×10^{-6}	$1.9 \pm 1.7 \times 10^{-4}$

The uncertainties correspond to ±2σ values.

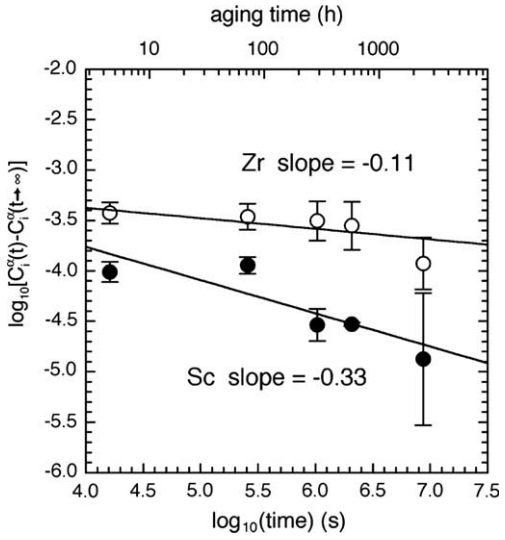

Fig. 13. Coarsening kinetics of an Al–0.09 Sc–0.047 Zr alloy as represented by a double-logarithmic plot of the Sc and Zr matrix supersaturations as a function of aging time at 300 °C. A total of 7,922,000 atoms were employed to construct this plot. The error bars in this plot represent $\pm 2\sigma$ values.

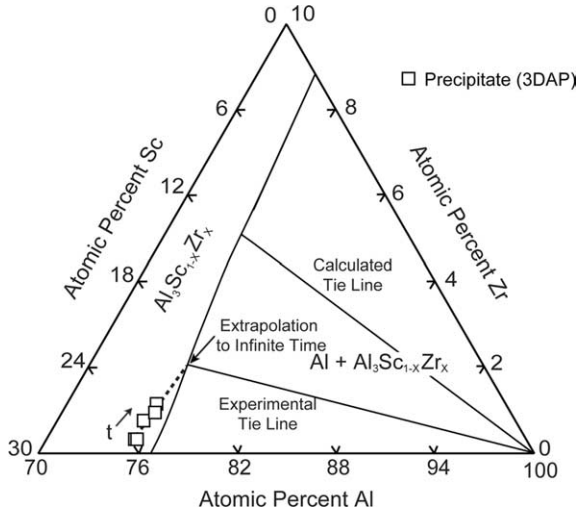

Fig. 14. Ternary phase diagram of Al–Sc–Zr system at 300 °C comparing the locations of experimental and calculated tie lines between the $Al_3Sc_{1-x}Zr_x$ precipitate and α-Al matrix phases of an Al–0.09 Sc–0.04 Zr alloy.

300 °C for 2412 h is 44 nm. Increasing the aging temperature to 375 °C and aging for 863.5 h, the root-mean-squared diffusion distance of Sc in Al is 10,582 and 204 nm for Zr, and the center-to-center interprecipitate distance is 292 nm. Thus, increasing the aging temperature from 300 to 375 °C reduces the percentage difference between the center-to-center interprecipitate distance and the root-mean-squared diffusion distance of Zr from 59% to 30%. At 300 °C, it is difficult to achieve simultaneously either a quasi-stationary state or stationary state for both Sc and Zr, within a reasonable time frame. Increasing the aging temperature to above 375 °C would make it easier to achieve either a quasi-stationary state or stationary state for both Sc and Zr, however precipitates would not remain coherent.

5.6. Extrapolation to infinite time

Since Al(Sc,Zr) alloys aged at 300 °C cannot achieve simultaneously either a quasi-stationary or stationary state within reasonable time frames for Sc and Zr, an extrapolation to infinite time is necessary to find differences between experimental and calculated tie-lines. Kuehmann and Voorhees [42] showed that the trajectory for the matrix composition follows the equilibrium tie-line, while the trajectory for the precipitate composition follows a straight line that is not parallel to the tie-line, assuming a quasi-stationary state is achieved. This extrapolation to infinite time is displayed on a ternary phase diagram at 300 °C, Fig. 14, utilizing the experimental coarsening data and the data from Fig. 2 for the $Al_3(Sc_{1-x}Zr_x)$ precipitate solvus line and the calculated tie-line. The intersection of the precipitate solvus line and the $Al_3(Sc_{1-x}Zr_x)$ precipitate composition extrapolation to infinite time (dotted line in Fig. 14) yields the experimental tie-line for Al–0.09 Sc–0.04 Zr. The deviation between the experimental and calculated tie lines is most likely due to a problem with the calculated solvus lines. Neglecting either the coherency stresses or metastable phases in the calculation of the solvus line possibly causes this inaccuracy.

6. Conclusions

Atom-probe tomography (APT) and high-resolution electron microscopy (HREM) are utilized to determine the temporal evolution of the nanostructure of an Al–0.09 Sc–0.047 Zr at.% alloy at 300 °C. The following results are obtained and discussed:

Table 6
Literature values for the diffusivity of Sc and Zr in Al

Solute elements	Method	D_0 ($m^2\ s^{-1}$)	Q (kJ mol^{-1})	References
Sc in Al	Tracer diffusivity	5.31×10^{-4}	174	[57]
	First-principle calculations	–	154	[63]
	Coarsening measurements	$(1.9 \pm 0.5) \times 10^{-4}$	164 ± 9	[7]
Zr in Al	Tracer diffusivity	7.28×10^{-2}	242	[58]
	Coarsening measurements	5.4×10^{-3}	222	[64]

- HREM (Fig. 3) images, taken along a [1 0 0] zone axis, show that $Al_3(Sc_{1-x}Zr_x)$ precipitates have facets parallel to the {1 0 0} and {1 1 0} planes when aged at 300 °C for times $\geqslant$288 h, in agreement with the morphology of Al_3Sc precipitates in a binary Al–Sc alloy [3,7,56]. Unlike the binary alloy, however, the Al(Sc,Zr) alloys do not have $Al_3(Sc_{1-x}Zr_x)$ precipitates that are completely facetted.
- Precipitate size distributions (PSDs) constructed from the HREM images are not self-similar, hence this basic assumption of coarsening models does not obtain.
- Increasing the aging temperature to 350 °C increases the solute–atom mobility and heterophase interfacial Zr segregation, which results in spheroidal precipitates. Spheroidal precipitates are attributed to a decrease in the α-Al/$Al_3Sc_{1-x}Zr_x$ {1 1 1} and {1 1 0} interfacial free energies to values close to that of the {1 0 0} facets, which is a result of the larger Zr diffusivity at 350 °C.
- For aging times $\geqslant$4.5 h, Sc-rich precipitates are observed in 3D atomic reconstructions (Figs. 6 and 8). The Sc concentration within the $Al_3(Sc_{1-x}Zr_x)$ precipitates decreases with a concomitant increase in Zr concentration (Table 3 and Fig. 12) as a function of aging time, which demonstrates directly that Zr is substituting for Sc within the $Al_3(Sc_{1-x}Zr_x)$ precipitates.
- The largest Zr concentration within $Al_3(Sc_{1-x}Zr_x)$ precipitates is 1.5 ± 0.2 at.% (Table 3), which is less than the calculated phase diagram value of 8.4 at.% Zr at 300 °C, Fig. 2. Also, the Zr concentration required to achieve the Al_3Zr phase (25 at.%) is not obtained. Aging at 300 °C, therefore, produces a metastable two-phase alloy consisting of an α-Al matrix and $Al_3(Sc_{1-x}Zr_x)$ ($L1_2$) precipitates.
- Zirconium segregates at the α-Al/$Al_3(Sc_{1-x}Zr_x)$ heterophase interface (Fig. 7), which is quantified by the relative Gibbsian interfacial excess of Zr with respect to Al and Sc, Γ_{Zr}^{Al-Sc} (Eq. (3)). Values of Γ_{Zr}^{Al-Sc} increase temporally, and reach a maximum value of 1.24 ± 0.62 atoms nm^{-2} after aging for 2412 h at 300 °C, Table 4. This interfacial excess corresponds to a decrease in the average interfacial free energy of 10 ± 5 mJ m^{-2}. The Zr segregation is at the periphery of the defined α-Al/$Al_3(Sc_{1-x}Zr_x)$ heterophase interface (Fig. 11), thus forming a Zr-rich concentric shell at or just inside this heterophase interface.
- Al_3Sc and/or $Al_3(Sc_{1-x}Zr_x)$ precipitates are postulated to nucleate heterogeneously on Sc–Sc, Sc–Zr or Zr–Zr dimers, which is followed by diffusion of Zr to Al_3Sc and/or $Al_3(Sc_{1-x}Zr_x)$ precipitates until the stoichiometric composition is ultimately achieved; the latter is not possible in a reasonable time frame because of the small diffusivity of Zr in α-Al relative to Sc in α-Al. The unraveling of the exact nucleation mechanism(s) involving solute dimers, requires detailed lattice kinetic Monte Carlo and cluster dynamic simulations [35].
- The depletion of the α-Al matrix concentrations of Sc and Zr yields the temporal evolution of an Al–0.09 Sc–0.047 Zr alloy. Fig. 12 demonstrates that the Sc concentration in the α-Al matrix decreases linearly after 4.5 h, while the Zr depletion commences at 72 h. The equilibrium solid-solubilities are calculated to be $1.2 \pm 0.3 \times 10^{-4}$ Sc and $1.9 \pm 1.7 \times 10^{-4}$ Zr at 300 °C, which are >15 times the values predicted by the calculated phase diagram. The time exponents for the decrease of the supersaturation (Eq. (5)) are calculated to be -0.33 for Sc and -0.11 for Zr (Fig. 13). The diffusivity of Sc in Al is considerably greater than that of Zr in Al and this is the reason why its time exponent is ca. $-1/3$.
- The asymptotic value for the Zr concentration (Eq. (1)) for an Al–0.09 Sc–0.047 Zr alloy is not achievable within reasonable time frames between 300 and 375 °C, because of the small diffusivity of Zr in Al.

Acknowledgments

This research was supported by the United States Department of Energy, Basic Energy Sciences Division, under contract DE-FG02-98ER45721. We thank David C. Dunand, Peter W. Voorhees, Alexander Umantsev, Emmanuelle A. Marquis, Dieter Isheim, Jens Alkemper, and Jason T. Sebastian for discussions and Olof Hellman for continuous development of *ADAM*, now named *APEX*. Special thanks are due to Argonne National Laboratory and especially Dr. Roseann Csencsits for use of the JEOL 4000EXII. We also thank Ashurst Inc. for supplying the Al–Sc master alloy and Robert W. Hyland, Jr. and Alcoa Inc. for supplying the Al–Sc and Al–Zr master alloys and for useful discussions.

References

[1] Fuller CB, Seidman DN. Acta Mater 2005;53:5415.
[2] Fuller CB. PhD Thesis, Northwestern University: Evanston, IL; 2003.
[3] Marquis EA. PhD Thesis, Northwestern University: Evanston. IL; 2002.
[4] Fuller CB, Seidman DN, Dunand DC. Scripta Mater 1999;40:691.
[5] Harada Y, Dunand DC. Acta Mater 2000;48:3477.
[6] Harada Y, Dunand DC. Microstructure and creep properties of Al_3Sc with ternary transition metal additions. In: The 7th International Conference on Creep and Fatigue at Elevated Temperature (Creep VII). Japan Society of Mechanical Engineers; 2001.
[7] Marquis EA, Seidman DN. Acta Mater 2001;49:1909.
[8] Fuller CB, Krause AR, Dunand DC, Seidman DN. Mater Sci Eng A 2002;A338:8.
[9] Marquis EA, Seidman DN, Dunand DC. Creep of precipitation strengthened Al(Sc) alloys. In: Mishra RS, Earthman JC, Raj SV, editors. Creep deformation: fundamentals and applications. Warrendale (PA): TMS; 2002. p. 299.
[10] Marquis EA, Seidman DN. Micros Microanal 2002;8:1100CD.
[11] Marquis EA, Dunand DC. Scripta Mater 2002;47:503.
[12] Harada Y, Dunand DC. Mater Sci Eng A 2002;329–331:686.
[13] Harada Y, Dunand DC. Scripta Mater 2003;48:219.
[14] Marquis EA, Seidman DN, Dunand DC. Acta Mater 2003;50:4021.
[15] Marquis EA, Seidman DN, Dunand DC. Microstructural and creep properties of an Al–2 Mg–0.2 Sc (wt.%) alloy. In: Jin ABZ, Bieler TA, Radhakrishnan B, editors. Hot deformation of aluminum alloys III. Warrendale (PA): TMS; 2003. p. 177.

[16] Fuller CB, Seidman DN, Dunand DC. Structure–property relationships of Al(Sc,Zr) alloys at 24 and 300 °C. In: Jin ABZ, Bieler TA, Radhakrishnan B, editors. Hot deformation of aluminum alloys III. Warrendale (PA): TMS; 2003. p. 531.
[17] Fuller CB, Seidman DN, Dunand DC. Acta Mater 2003;51:4803.
[18] Marquis EA, Seidman DN, Dunand DC. Acta Mater 2003;51:4751.
[19] Marquis EA, Seidman DN, Asta M, Woodward CM, Ozolin V. Phys Rev Lett 2003;91:036101.
[20] Marquis EA, Seidman DN, Asta M, Woodward C. Acta Mater 2005, doi:10.1016/jactamat.2005.08.035.
[21] Marquis EA, Seidman DN. Acta Mater 2005;53:4259.
[22] Karnesky RA, Meng L, Seidman DN, Dunand DC. Mechanical properties of a heat-treatable Al–Sc alloy reinforced with Al_2O_3 disperoids. In: Affordable metal matrix composites for high performance applications II. Pittsburgh (PA): TMS; 2003. p. 215.
[23] van Dalen ME, Dunand DC, Seidman DN. Precipitate strengthening in Al(Sc,Ti) alloys. In: Affordable metal matrix composites for high performance applications II. Pittsburgh (PA): TMS; 2003. p. 195–201.
[24] Hyland RW. Metall Trans A 1992;23A:1947.
[25] Murray JL. J Phase Equilib 1998;19:380.
[26] Elagin VI, Zakharov VV, Pavlenko SG, Rostova TD. Phys Met Metallogr 1985;60:88.
[27] Toropova LS, Kamardinkin AN, Kindzhibalo VV, Tyvanchuk AT. Phys Met Metallogr 1990;70:106.
[28] Kamardinkin AN. Russ Metall 1991;2:216.
[29] Harada Y, Dunand DC. Scripta Mater 2002;329–331:686.
[30] Touloukian YS, Kirby RK, Taylor RE, Desai PD. Thermophysical properties of high temperature solid materials. New York (NY): Macmillan; 1967. p.2.
[31] Vegard L. Z Phys 1921;5:17.
[32] Vetrano JS, Henager CH. Micros Microanal 1999;160.
[33] Tolley A, Radmilovic V, Dahmen U. Scripta Mater 2005;52:621.
[34] Forbord B, Lefebvre W, Danoix F, Hallem H, Marthinsen K. Scripta Mater 2004;51:333.
[35] Clouet E. PhD Thesis, École Centrale Paris; 2004.
[36] Royset J, Ryum N. Inter Mater Rev 2005;50:19.
[37] Lifshitz IM, Slyozov VV. J Phys Chem Solids 1961;19:35.
[38] Wagner C. Z Elektrochem 1961;65:581.
[39] Wagner R, Kampmann R, Voorhees P. Homogeneous second-phase precipitation. In: Kostorz G, editor. Phase tranformations in materials. New York (NY): Wiley-VCH; 2001. p. 309.
[40] Ratke L, Voorhees PW. Growth and coarsening: ripening in materials processing. Berlin: Springer; 2002.
[41] Umantsev A, Olson G. Scripta Metall 1993;29:1135.
[42] Kuehmann CJ, Voorhees PW. Metall Mater Trans A 1996;27A:937.
[43] Murray J, Peruzzi A, Abriata JP. J Phase Equilib 1992;13:277.
[44] Hellman OC, Vandenbroucke JA, Rüsing J, Isheim D, Seidman DN. Microsc Microanal 2000;6:473.
[45] Hellman OC, Vandenbroucke JA, Rüsing J, Isheim D, Seidman DN. Identification of 2D boundaries from 3D atom probe data, and spatial correlation of atomic distributions with interfaces. In: Lassila DH, Phillips R, Devincre B, editors. Multiscale phenomena in materials – experiments and modeling. Mater Res Soc Sympos Proc 2000;578:395.
[46] Sebastian JT, Hellman OC, Seidman DN. Rev Sci Instrum 2001;72:2984.
[47] Hellman OC, Vandenbroucke J, Blatz du Rivage J, Seidman DN. Mater Sci Eng A 2002;327:29.
[48] Hellman OC, Seidman DN. Mater Sci Eng A 2002;A327:24.
[49] Hellman OC, Blatz du Rivage JB, Seidman DN. Ultramicroscopy 2003;95:199.
[50] Yoon KE, Isheim D, Noebe RD, Seidman DN. Interf Sci 2002;9:249.
[51] Isheim D, Seidman DN. Mater Sci Eng A 2002.
[52] Brailsford AD, Wynblatt P. Acta Metall 1979;27:489.
[53] Defay R, Prigogine I, Bellemans A. Surface tension and absorption. New York (NY): Wiley; 1966.
[54] Dregia SA, Wynblatt P. Acta Metall Mater 1991;39:771.
[55] Krakauer BW, Seidman DN. Phys Rev B 1993;48:6724.
[56] Asta M, Ozolins V, Woodward C. JOM 2001;53:16.
[57] Fujikawa SI. Defect Diff Forum 1997;143–147:115.
[58] Hirano K, Fujikawa S. J Nucl Mater 1978;69–70:564.
[59] Robson JD. Acta Mater 2004;52:1409.
[60] Kampmann R, Wagner R. Materials Science and Technology, vol. 5. Weinheim: VCH; 1991.
[61] Krakauer BW, Seidman DN. Acta Mater 1998;17:6145.
[62] Asta M, Foiles SM, Quong AA. Phys Rev B 1998;57:11265.
[63] Asta M, Ozolins V. unpublished results.
[64] Zedalis MS, Fine ME. Metall Trans A 1986;17A:2187.